Efficient Carrier Separation and Intriguing Switching of Bound Charges in Inorganic–Organic Lead Halide Solar Cells

7 AUTHORS, INCLUDING:

Gee Yeong Kim
Ewha Womans University

17 PUBLICATIONS   **41** CITATIONS

SEE PROFILE

Hyun Suk Jung
Kangwon National University

208 PUBLICATIONS   **3,329** CITATIONS

SEE PROFILE

Efficient Carrier Separation and Intriguing Switching of Bound Charges in Inorganic−Organic Lead Halide Solar Cells

Gee Yeong Kim,[†] Seol Hee Oh,[†] Bich Phuong Nguyen,[†] William Jo,*,[†] Byeong Jo Kim,[‡] Dong Geon Lee,[‡] and Hyun Suk Jung[‡]

[†]Department of Physics, Ewha Womans University, Seoul 120-750, South Korea
[‡]School of Advanced Materials Science & Engineering, Sungkyunkwan University, Suwon 440-746, Korea

Ⓢ Supporting Information

ABSTRACT: We fabricated a mesoporous perovskite solar cell with a ∼14% conversion efficiency, and we investigated its beneficial grain boundary properties of the perovskite solar cells through the use of scanning probe microscopy. The $CH_3NH_3Pb(I_{0.88},Br_{0.12})_3$ showed a significant potential barrier bending at the grain boundary and induced passivation. The potential difference value in the $x = 0.00$ sample is ∼50 mV, and the distribution of the positive potential is lower than that of the $x = 0.12$ sample. We also investigated the polarization and hysteretic properties of the perovskite thin films by measuring the local piezoresponse. Specifically, the charged grain boundaries play a beneficial role in electron−hole depairing and in suppressing recombination in order to realize high-efficiency perovskite solar cells.
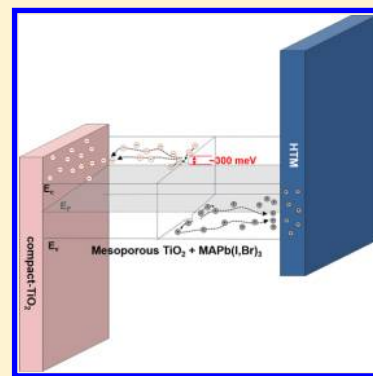
Methylammonium (MA) lead halide perovskites have been considered to be promising photovoltaic materials due to their large absorption coefficient, high carrier mobility, high carrier diffusion length, and direct band gap.[1−3] The triiodide absorber has an electron−hole diffusion length of ∼100 nm, and the planar heterojunction perovskite solar cell in the mixed halide perovskite has a 1 μm diffusion length.[4] $CH_3NH_3PbI_3$ has a direct band gap of 1.55 eV, which is consistent with absorption near the 800 nm wavelength. It also has a weak binding energy of about 0.030 eV to produce excitons. The excitons separate rapidly out the free carriers at room temperature.[5−7] The power conversion efficiency (PCE) of perovskite has increased, from 3.8% in 2009 to 19.3% at present, through optimizations of the perovskite solar cell structure that have been achieved through various preparation methods and with different compositions.[2,8−10] The morphology, thickness, and light-harvesting properties of the perovskite material are primary factors that have been found to improve the PCE, and in addition, perovskite solar cells have another advantage in that the band gap of $CH_3NH_3X_3$ (MA: CH_3NH_3; X: halogen) can be controlled by substituting the I with Br ions from 1.57 to 2.29 eV.[11−13] Seok and his colleagues at KRICT have also reported that the lattice parameter of $MAPb(I_{1−x}Br_x)_3$ ($0 \leq x \leq 1$, x: ratio of I and Br elements) exhibits a linear correlation with the Br concentration as a result of switching the larger I with smaller Br atoms, thereby reducing the lattice spacing.[14] Optimal cells were fabricated from $x \approx 0.2$, and these exhibit a high conversion efficiency and a better stability. However, an understanding of their physical mechanism and electronic effects with respect to the Br concentration in perovskite solar cells is still lacking. The physical properties of

the Br-containing perovskite films have yet to be determined. The Br-containing perovskite films induce changes in the crystal structure and in the optical band gap, and as a result, the recombination process is affected and determines the V_{OC} of the devices. The Yang and Green groups have recently suggested that the grain boundaries (GBs) in planar perovskite solar cells have beneficial effects.[15,16] The potential barrier assists in the photoexcited carrier separation and suppresses recombination due to the passivation at the GBs. However, understanding of the electrical properties of the GBs in mesoporous $MAPb(I,Br)_3$ films with various Br compositions has yet to be provided. Therefore, we have investigated the role that the GBs play in mesoporous perovskite solar cells. In this work, the GB of the perovskite film was characterized via Kelvin probe force microscopy (KPFM) and conductive atomic force microscopy (C-AFM) in order to investigate their roles in a $TiO_2/MAPb(I_{1−x}Br_x)_3$ heterojunction device with different Br ratios. Many experimental and theoretical studies have reported that GBs in perovskite solar cells do act as a recombination center. Yin et al. reported that GBs are intrinsically beneficial in halide perovskites, and these do not generate any gap states as in a single crystal through a first-principles calculation.[17] Σ5 (310) and Σ3 (111) GBs in $MAPbI_3$ are free from defect states and are thus electrically benign. Meanwhile, the intrinsic GBs of GaAs, CIGS, CZTSe, and CdTe generate deep levels in the band gaps. These deep levels are harmful for the device
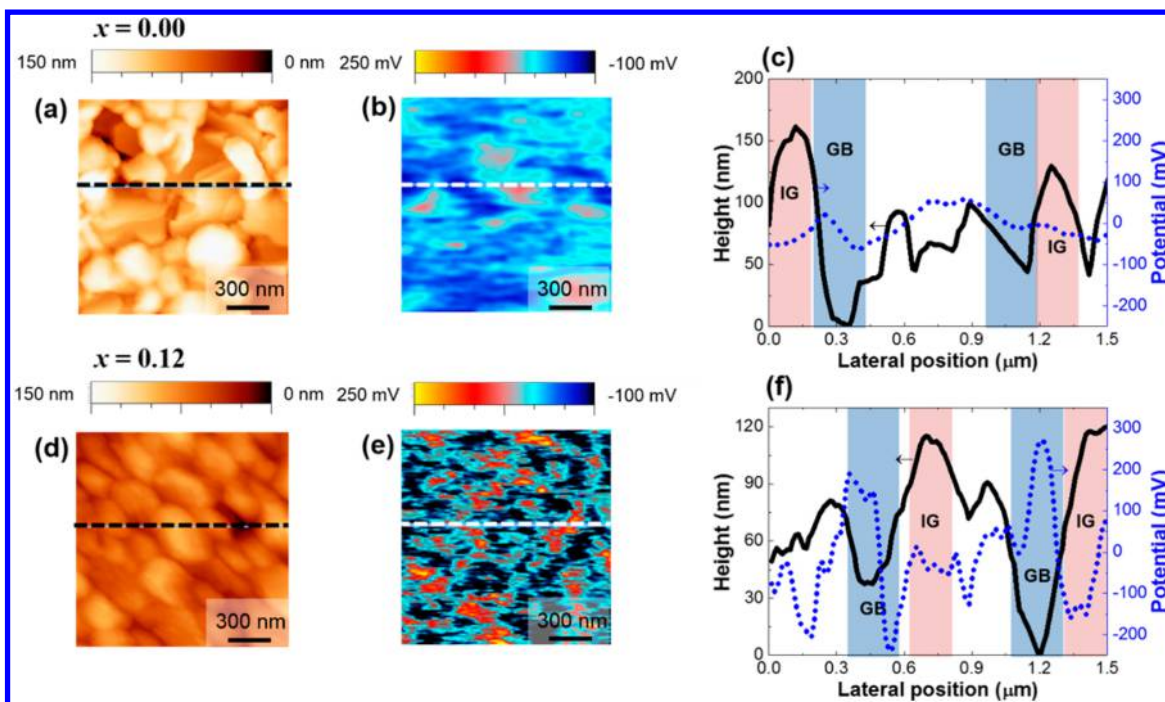
Figure 1. KPFM measurements were performed on a $CH_3NH_3Pb(I_{1-x}Br_x)_3/TiO_2/FTO/glass$. (a,d) Topography images and (b,e) surface potential images of the corresponding topography. The GB regions can be easily separated based on the reverse topography images. In the $x = 0.12$ sample, a positive surface potential is indicated at the GB, and a negative potential is exhibited on the surface of the IGs. (c,f) One-dimensional potential and the topography line profiles near the GBs in the perovskite thin films. The region of the line profiles is marked in (a) and (d). The potential value at the GBs is ~280 mV, and that at the IGs is −150 mV in the $x = 0.12$ sample.

performance. However, it is still unclear what the roles of the GBs are in the $MAPb(I_{1-x}Br_x)_3$ in terms of experimental results of the electrical properties of GBs. Recently, deQuilettes et al. reported that GBs are not benign based on photoluminescence (PL) and fluorescence microscopy. GBs in $CH_3NH_3PbI_3(Cl)$ films show ~65% lower PL intensity and shorter local PL lifetimes at GBs than grains.[18] Consequently, GBs in $CH_3NH_3PbI_3(Cl)$ exhibited faster nonradiative decay. Even though the elements in the Letter are not I and Br, the implications on GBs are serious and interesting. We have to study further the role of halogen ions on the passivation in the GBs and the surfaces.

Figure 1 presents the mapping images of the topography and surface potential on a $MAPb(I_{1-x}Br_x)_3/TiO_2/FTO/glass$ obtained using KPFM measurements in the dark. The cross-sectional image of the mesoporous $MAPb(I_{0.88}Br_{0.12})_3$ film is indicated in Supporting Information Figure S1. The $x = 0.12$ sample exhibits a high potential value at the GBs and low potential value at the intragrains (IGs), as shown in Figure 1e. However, a large potential difference is not present at the GBs and the IGs in the $x = 0.00$ sample without Br, as shown in Figure 1b. The details of the potential value are used to obtain the line profiles, as shown in Figure 1c and f. The line profiles exhibit a one-dimensional potential and topography line profiles near the GBs. The regions of the line profiles are marked in Figure 1a and d. In the $x = 0.12$ sample, a high positive surface potential is indicated at the GB, and a negative potential is present at the IGs. The potential value at the GB is ~300 mV, and that of the IG is −150 mV. However, the $x = 0.00$ sample does not display a large potential difference between the GBs and the IGs. The potential difference value in the $x = 0.00$ sample is ~50 mV, and the distribution of the positive potential is lower than that of the $x = 0.12$ sample.

Supporting Information Figure S2 shows the histograms of the potential value for the perovskite thin films with different Br composition ratios. The potential range was higher for the $x = 0.12$ Br film than that for the $x = 0.00$ film. Most of the potential values in the $x = 0.00$ sample were ±50 mV. However, the potential value was high for the $x = 0.12$ sample at about 90 mV. The potential value of the perovskite has a similar potential barrier value as the CIGS or CZTSe thin films. Moreover, we analyzed the potential variations of the IGs and GBs, as indicated in Supporting Information Figure S3. Our group reported the local electrical properties of the GBs in CIGS and CZTSe thin film solar cells.[19,20] The potential values of the CIGS and the CZTSe indicate a potential barrier from 100 to 300 mV at the GBs. It has a similar potential value as GBs in the perovskite $MAPb(I_{1-x}Br_x)_3$ thin films. Persson et al. reported that the potential barrier in CIS thin films forms an absence of holes inside of the GB, which suppresses recombination near the GBs.[21] The potential barrier is derived from the Cu vacancy near the GBs. In perovskite solar cells, the GBs also indicate positively charged regions, and therefore, the GBs consequently drive the negative energy band bending as for the CIGS or CZTSe thin films. Dymshits et al. measured the potential difference at the perovskite GBs with a value of 25 mV.[22] The potential barrier in the perovskite GBs discloses the hole accumulation and could play a minor effect in the performance of the solar cells.[22] The potential value at the GBs of this group is very different from ours due to the difference in the n-type layer (to clarify, the measurement conditions like tip materials, operational frequency, scan speed, etc.). Moreover, the efficiency of the perovskite solar cell that they measured is lower than that of our perovskite solar cells. The positively charged GBs in the $x = 0.12$ of the perovskite thin film induce a higher local built-in potential at the GBs. The high local built-in

potential at the GBs prompts downward energy band bending, and this electrical property near the GBs is similar to that of polycrystalline thin-film solar cells, such as CIGS and CZTSe.[19−21,23−25] In CIGS thin-film solar cells, the local built-in potential leads to a minority carrier of the electrons attracting the GBs and extruding the majority carriers of the hole carriers to the IGs. Thus, the downward energy band bending at the GBs assists in electron−hole carrier separation and suppresses recombination. These local electrical properties also appear in the perovskite solar cells. We observed the value of the potential barrier to be ~300 mV and demonstrate electron carrier transport near the GBs in $MAPb(I_{0.88},Br_{0.12})_3$, as indicated in Figure 1f. The electrons are attracted to the GBs and move to the TiO_2 layer, and the holes are repelled from the GBs and are driven to the hole transport layer. The high efficiency observed in the $x = 0.12$ sample indicates a comparatively large potential difference at the GBs and IGs in the absorber layer. Therefore, we can expect similar beneficial electrical properties in the perovskite solar cells, such as the polycrystalline thin-film solar cells. On the other hand, Chen et al. reported on a controllable passivation technique for planar perovskite films.[15] The PbI_2 phase appeared in the GBs of the perovskite films by thermal annealing. Consequently, the PbI_2 phase alters the grain to GB energy band bending downward (~50 mV) to upward (~30 mV), and the carrier recombination is reduced near the GBs. Therefore, PbI_2 effectively passivates the grain and improves the performance of the device.[15] However, the results for the mesoporous perovskite films are different from those of the planar perovskite thin-film results.

Figure 2 shows the topography and the local current images that were obtained with C-AFM measurements in a dark condition. The grain size of the surface is of several hundred nanometers, and the images of the local current map were observed by applying a positive voltage bias of 0.2, 0.6, and 1.0 V to the samples in the dark. The topography and SEM images of the $x = 0.00$ and 0.12 films are shown in Supporting Information Figure S4. The scan size of the AFM images is 5 × 5 μm^2. The $x = 0.00$ film shows a slightly larger grain size of around 300−600 nm than $x = 0.12$ films at around 200−500 nm. The root-mean-square (RMS) roughness of the $x = 0.00$ and 0.12 films is 19.71 and 26.88 nm, respectively. In the $x = 0.12$ sample, some voids in the corner of grains are found, which might lead to a difference in conducting behaviors in the perovskite cells.

For the $x = 0.12$ sample, local current routes form through the GBs and some of the grains in the perovskite thin film. The current value is less than 50 pA, as indicated in Figure 2j−l. However, the $x = 0.00$ samples present a local current flow through some of the grains when applying an external bias. The current for the $x = 0.00$ sample greatly increases to higher than 0.6 V at the spatial regions, as indicated in Figure 2e and f. We also observed the destruction of the topography in the $x = 0.00$ sample by applying an external bias higher than 0.6 V. Thus, the morphology of the perovskite layer was different when applying an external bias of 1 V to the sample, as shown in Figure 2c. However, the $x = 0.12$ sample indicates that the morphology is the same after applying an external bias of 1 V.

Figure 3 displays the line profiles of the topography and the corresponding local current value. The regions of the line profiles are indicated in Figure 2. A high local current flows through the grains, and the current value is similar to the $x = 0.00$ and 0.12 samples under a 0.2 V bias. However, the current
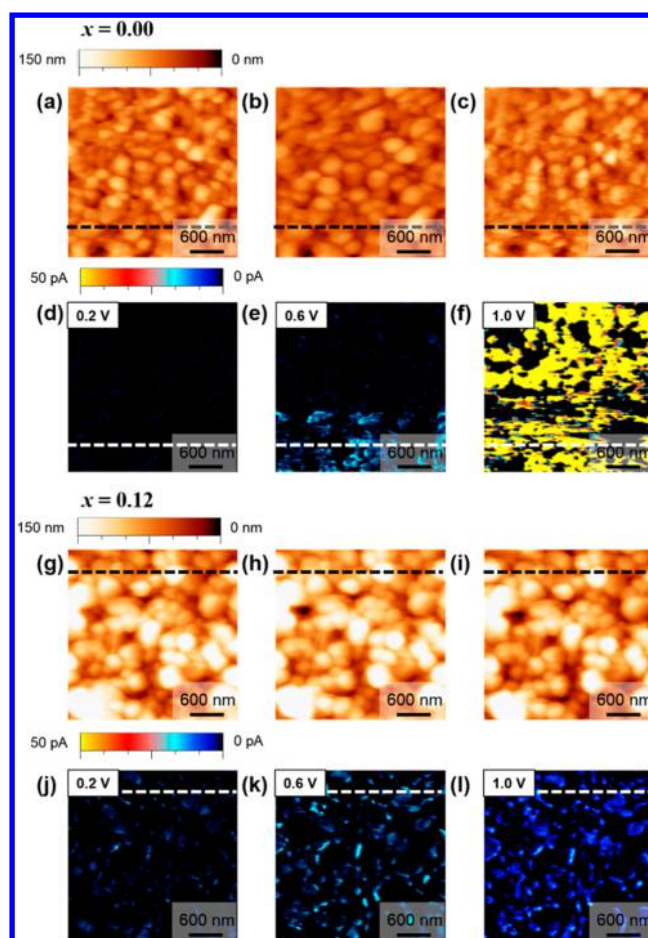

Figure 2. (a−c) $x = 0.00$ and (g−i) $x = 0.12$ show topography images of the films. (d−f) and (j−l) Corresponding local current mapping images when an external bias of 0.2, 0.6, and 1 V, respectively, is applied to the samples. For $x = 0.12$, the film shows local current flows through most of the grains in the film surface. However, the $x = 0.00$ film exhibits partial local current flows near the grains. The Br-containing perovskite film exhibits a conduction channel near the grains and the GBs.

of the $x = 0.00$ sample is ~200 pA, which is 10 times higher than that of the $x = 0.12$ sample when applying 1 V. Moreover, the current flows for all grains and GBs of the $x = 0.00$ sample under 1 V of bias, as indicated in Figure 3c. The morphology of the samples was changed with an applied external bias, as shown in Figure 2. It could have originated from the ionic migration or bound charge inside of the surfaces. In a previous study, Shin et al. and Kim et al. obtained the current value for the GBs in the CIGS and CZTSSe thin films of ~1 nA.[26,27] We can predict that the reason for a lower local current value in the $MAPb(I,Br)_3$ thin film is the presence of the mesoporous TiO_2 layer. The region with a difference in the current value for the $x = 0.00$ sample originated from the ununiform coating condition between the TiO_2 and the perovskite layer. The value of the flowing current is ~20 pA, which is lower than the polycrystalline CIGS or the CZTSSe thin films. Yun's group proposed that the higher current around the GBs could induce the decrease in the V_{OC} by formation a shunt path.[16] The $x = 0.00$ sample has high local current flow grains and GBs by applying an external bias relative to the $x = 0.12$ sample. Suarez et al. reported that an absorption band edge for shorter wavelengths was obtained by increasing the Br ratio (x) in
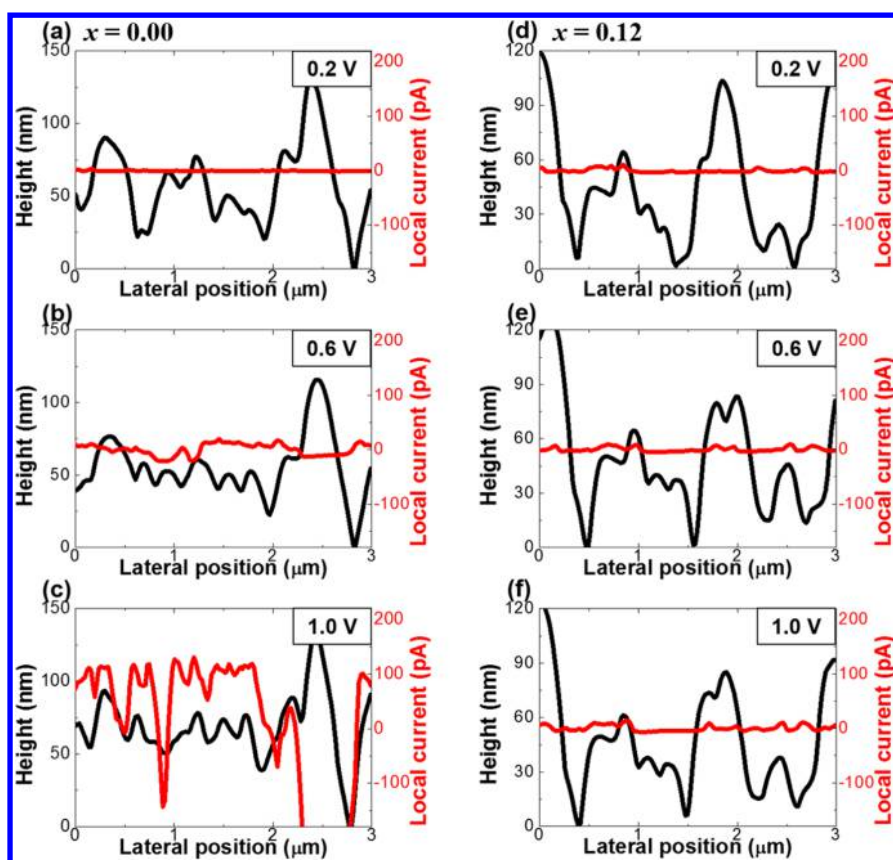
Figure 3. One-dimensional line profiles of the perovskite films with different Br concentrations. (a–c) $x = 0.00$ and (d–f) $x = 0.12$ show the local current. In the case of $x = 0.00$, the current shows an extreme increase of ~200 pA by applying an external bias of 1 V. However, the $x = 0.12$ film indicates current flows of ~30 pA.

MAPb$(I_{1-x}Br_x)_3$.[28] Hence, the band gap when using Br instead of I for the MAPb$(I_{0.88}Br_{0.12})_3$ sample results in a broader band gap. In addition, the insertion of the Br in the perovskite lattice diminishes the charge recombination in the absorber layer of the film, and thus, the Br determines the V_{OC} of the device by slightly improving the lifetime of the devices.[28] As a result, the improved V_{OC} could be inhibited in the recombination.

Perovskite solar cells generally have an issue with hysteresis in the $J-V$ measurements. Hysteresis effects are created from an incorrect estimation of the efficiency. Wei et al. reported that the hysteresis in perovskite solar cells originates from the ferroelectric effect.[29] They found that the various architectures of perovskite devices exhibit different hysteretic behaviors, and these could be associated with domain wall motions, which in turn are affected by the grain size of the perovskite films. Moreover, the ferroelectric effects influence the properties of the perovskite solar cells.[29] Fan et al. investigated the ferroelectricity of the MAPbI$_3$ perovskite.[30] They found that the polarization magnitude was ~8 μC/cm^2 through first-principles calculations. In their experiments, the PFM measurements indicate that the perovskite solar cells (MAPbI$_3$) are not ferroelectric at room temperature. There were significant variations in the amplitude and phase images under a DC poling voltage of +2.5 V, and they suggested that polarization could form as a result of the orientation polarization of the MA$^+$ dipole. However, they could not observe the amplitude hysteresis loop to have any butterfly shape. As a result, they suggested that the MAPbI$_3$ does not exhibit ferroelectricity at room temperature. The ferroelectric properties of the perovskite are an essential issue. However, no study has reported on

the PFM characteristics of MAPb(I,Br)$_3$ mesoporous perovskite film. Therefore, we investigated the ferroelectricity and polarization properties of the perovskite solar cells. PFM measurements are largely used to characterize the ferroelectric domains in the ferroelectric materials at the nanoscale.

Figure 4 shows PFM images of the $x = 0.12$ film in terms of the (a) topography, (b) amplitude, (c) phase, and (d) local hysteresis loop. Different amplitudes and phase signals can be observed at the spatial grain and GBs. The phase signal of the $x = 0.12$ sample shows a relatively small difference. We also observed a local well-saturated hysteretic loop in the grain of the film, which indicates hysteretic behavior and possible polarization switching of the MAPb$(I_{0.88}Br_{0.12})_3$, in a manner similar to that for MAPbI$_3$ reported by Kutes et al.[31] We obtained a local $P-E$ loop that had a shape like that of conventional perovskite Pb-based or Bi-based oxide ferroelectrics.[32,33] However, we could not obtain the poling characteristics in the domains of the MAPb$(I_{0.88},Br_{0.12})_3$ perovskite thin films when a DC bias of 10 V was applied with a low-phase signal. Fan et al. proposed that polarization switching and the change in the phase and amplitude resulted from electrochemical phenomena.[30] We can also expect that polarization switching originates from the ionic replacement and the ionic conductivity of the materials. Therefore, we have to carefully conclude whether the MAPb(I,Br)$_3$ material is ferroelectric or not. In a recent report, Stoumpos et al. observed a hysteretic behavior in bulk single crystals of β-MAPbI$_3$.[34] Moreover, Kutes et al. suggested the presence of ferroelectric domains in the high-quality solution-processed MAPbI$_3$ perovskite thin films.[31] They measured the perovskite films
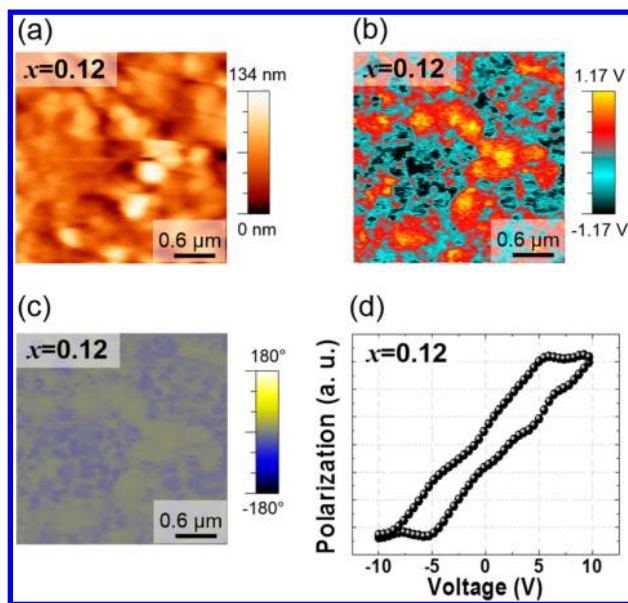
Figure 4. PFM images of the $x = 0.12$ film. (a) Topography, (b) amplitude, (c) phase, and (d) local hysteresis loop. Different amplitudes and phase signals can be observed at the spatial grain and at the GBs. However, the variation in the phase signals is too small.

and found evidence for the reversible switching of the ferroelectric domains by poling with a DC bias through PFM measurements.[31] Frost et al. suggested that internal electrical fields related to polarization domains influence the hysteresis of the $J-V$ curves of the perovskite solar cells.[35] The hybrid perovskites have a natural electric polarization, and the presence of the ferroelectric domains will prompt the internal electric potential "ferroelectric domain" that may help carrier separation and reduction in the recombination of the photogenerated electron and hole. This also contributes to the improvement of the V_{OC} and the current–voltage hysteresis in the perovskite solar cells.[35] In perovskites, Beilsten-Edmands et al. reported that perovskite $CH_3NH_3PbI_3$ is not ferroelectric and the origin for the hysteretic behavior in their solar cells is something different like ionic migration.[36] The hysteresis loop of the $CH_3NH_3PbI_3$ film looks very similar to the ferroelectric material, but the magnitude of the hysteresis charge density surpasses 1000 μC cm^{-2}. The gigantic magnitude of the charge density manifests nonferroelectricity because large polarization used to be relevant to leaky behaviors. Therefore, the effects of the hysteretic conduction result from the ionic migration and the associated charged trapping.[36] It is still under debate whether the ferroelectric polarization is related to hysteresis in the $J-V$ curves. In our PFM studies, we can expect that polarization switching originates from various origins like (1) ionic replacement into defects, (2) ionic conductivity, (3) interface charge trapping, as well as (4) ferroelectricity-related bound charge polarizations. Therefore, we have to carefully conclude that at the moment, the $MAPb(I,Br)_3$ material is not firmly proved yet as ferroelectric but has a structural phase transition that should be dominant as (1) order–disorder or (2) displacement type. To demonstrate ferroelectricity, we need to perform more fundamental experiments like dielectric measurements.

Furthermore, we established hysteresis behaviors in our cells. Supporting Information Figure S5 shows the photovoltaic

performance with respect to the scan direction of the $x = 0.00$ and 0.12 perovskite solar cells. The efficiency of the reverse scan is 10.63%, and the forward scan is 7.47%, as indicated in Supporting Information Figure S5a. The best-performing cell ($x = 0.12$) has a current density of 18.64 mA/cm^2, an open-circuit voltage of 1.02 V, a fill factor of 0.72, and a conversion efficiency of ∼13.6%, as shown in Supporting Information Figure S5b. Our cell has a strong hysteric behavior in the $J-V$ curve, as shown in Supporting Information Figure S5a. This could have originated from the nonuniform perovskite film.[37] The transient behavior generates the hysteresis corresponding with the polarization response of the perovskite absorber layer, which leads to the change in the photocurrent extraction efficiency of the cells.[38] On the basis of our characterization, there is no direct evidence of ferroelectricity in perovskite materials even though the hysteretic behavior in $J-V$ curves and the bound charge motion in the PFM measurement are observed. We need to investigate more carefully and systematically the characteristics and the polarizing tendency and elucidate the origin in terms of fundamental materials properties and extrinsic diffusion or defects. The GBs in the perovskite film are reported to show similar electrical properties to the polycrystalline CIGS and CZTSe thin-film solar cells by several groups. However, no hysteretic behaviors in $J-V$ curves have been reported in the CIGS and CZTSe solar cells.

We predict a band diagram near the GBs and in the electron–hole carrier transport inside of the $MAPb(I_{0.88},Br_{0.12})_3$ film based on the KPFM and C-AFM measurements. Figure 5a shows the description of the three-dimensional structure of the compact TiO_2, mesoporous-TiO_2, and perovskite absorber layer. We characterized the electrical properties of the perovskite layer via KPFM, C-AFM, and PFM measurements. On the basis of these results, we can expect a band diagram near the GBs in the mesoporous $MAPb(I_{0.88},Br_{0.12})_3$ perovskite thin film, as shown in Figure 5b. The GBs in the perovskite absorber layer could improve the electron–hole carrier separation. The charged GBs form downward energy band bending, which helps the electron move to the TiO_2 layer and the hole become attracted to the perovskite and hole transport layer. Thus, the electron–hole carrier efficiently dissociates with the n-type TiO_2 layer and the p-type HTM layer. The $MAPb(I_{0.88}Br_{0.12})_3$ film shows a relatively higher potential barrier than the $MAPbI_3$ at the GBs. There, we can predict that the Br inside of the $MAPbI_3$ induces a high potential barrier and induces the downward band bending. This results in a reduction in the recombination near the GBs. Moreover, none of the GBs in the perovskite film have any deep states in the $MAPbI_3$, as evidenced by the first-principles calculations; therefore, we can expect that the GBs do not act as recombination centers.[17] We assessed the Br and I composition distribution via energy-dispersive X-ray spectroscopy (EDS) mapping to determine the Br effects in the $MAPbI_3$ film. Supporting Information Figure S6 shows the plain view and EDS mapping images of the $MAPb(I_{0.88}Br_{0.12})_3$ samples deposited on mesoporous TiO_2 films with $x = 0.12$. The morphology of the $x = 0.12$ perovskite layer consists of a uniform grain size of several hundred nanometers and a dense surface. The EDS mapping of the I and Br elements of the perovskite films with $x = 0.12$ shows that the I and Br elements are uniformly located on the film. We overlapped the SEM and EDS mapping images, and the Br elements do not gather near the GB or IG of the film surface.
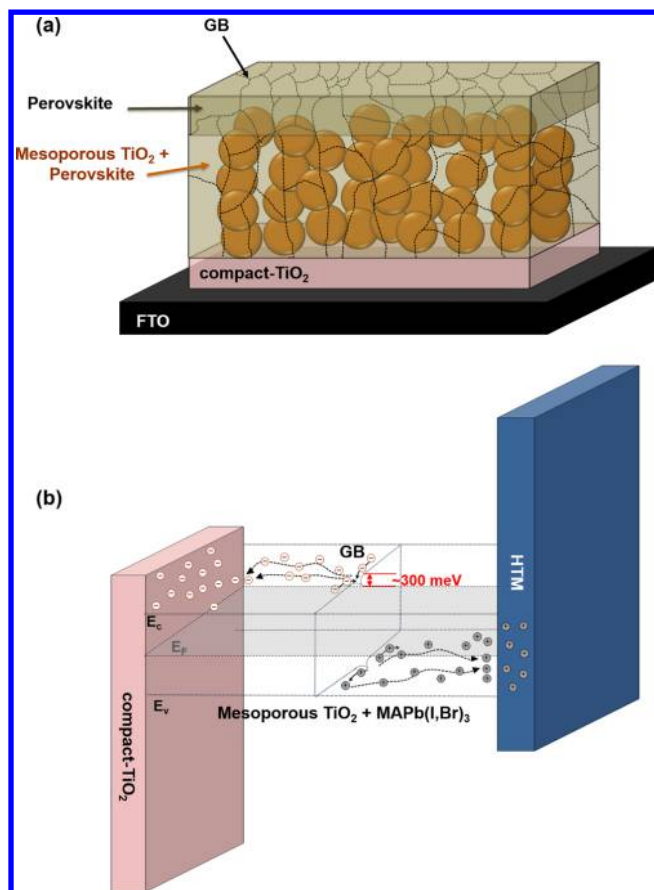
Figure 5. (a) Structure of the mesoporous TiO_2 with a mixed halide perovskite absorber. We characterized the electrical properties of the perovskite absorber via KPFM, C-AFM, and PFM. (b) The schematic band diagram near the GBs in Br-contained $MAPb(I_{0.88},Br_{0.12})_3$ thin films. The electron−hole carrier separates the mesoporous TiO_2 layer from the perovskite layer. The charged GBs (potential value at GBs ~300 mV) have a high local built-in potential, which improves the carrier separation. The electrons attract the TiO_2 layer, and the holes move to the HTM layer.

In summary, we characterized the local electrical properties of the $MAPb(I_{1−x}Br_x)_3$ perovskite thin films. The KPFM and C-AFM results show that a high, positively charged region appeared in the GBs and the local current (<50 pA) flows through most of the grains in the x = 0.12 of perovskite thin films. Br-containing perovskite thin films show electrical properties similar to those of polycrystalline CIGS and CZTSSe thin-film solar cells. Moreover, we also examined the hysteretic polarization properties of the Br-containing perovskite films. The films show a higher spot size in the domains relative to the grain size. Therefore, we can expect positively charged GBs to play a beneficial role in the perovskite thin-film solar cells by improving the electrical quality characteristics, such as the carrier collection and recombination.

■ EXPERIMENTAL METHODS

The $CH_3NH_3I_3$ and PbI_2 (or PbI_2 and $PbBr_2$, Aldrich) for a 0.8 M $CH_3NH_3Pb(I_{1−x}Br_x)_3$ (x = 0.15, nominal) solution were dissolved in a mixture of γ-butyrolactone and dimethyl sulfoxide (7:3 v/v) at 60 °C for 12 h.[14] The prepared $CH_3NH_3Pb(I_{1−x}Br_x)_3$ was coated onto the glass/FTO/blocking-TiO_2/mesoporous-TiO_2 (F-doped SnO_2; FTO, Dyesol, TEC 15) and was then placed on a 100 °C hot plate for 20 min.

The hole transport layer was prepared with 80 mg of 2,20,7,70-tetrakis(N,N-dipmethoxyphenyl-amine)-9,90-spirobifluorene (spiro-MeOTAD), 8.4 mL of 4-*tert*-butylpyridine, and 51.6 mL of bis(trifluoromethane)sulfonamide lithium salt (Li-TFSI) dissolved in 1 mL of chlorobenzene. These materials were then spin-coated at 2500 rpm for 45 s. Noh et al. reported that the $MAPb(I_{1−x}Br_x)_3$ ($x \geq 0.2$) solar cells exhibited a stable efficiency under high humidity, which could be the result of the cubic-phase-based cells that improve the stability rather than the tetragonal-phase $MAPb(I_{1−x}Br_x)_3$ ($x < 0.2$) based cells.[14] In addition, the $x \geq 0.2$ of perovskite cells inhibits the loss of the J_{SC} in the device. Thus, we used x = 0.12 for the Br concentration (the measured Br concentration is x = 0.12). All of the processes were carried out under controlled atmospheric conditions with humidity of <0.5 ppm. Finally, a 100 nm thick Ag electrode was deposited with a shadow mask by thermal evaporation at $10^{−6}$ Torr.[39,40] The morphology of the perovskite surface was obtained by scanning probe microscopy, and elemental mapping was carried out via energy-dispersive X-ray spectroscopy (EDS) (FE-SEM, JEOL, JSM-6700F). The electrical characterization was performed using KPFM, C-AFM, and PFM measurements taken using a commercial atomic force microscope (AFM) (Nanofocus Inc., n-Tracer). For KPFM and C-AFM, Pt/Ir-coated silicon cantilevers (Nanosensor Inc.) were used, while for PFM, Co-coated silicon cantilevers (Nanosensor Inc.) were used. The topographical images and the electrical signals were always measured simultaneously. KPFM was measured in a noncontact mode by applying an AC voltage with an amplitude of 1.0 V and a frequency of 70 kHz. The scan size of the images was 3×3 μm^2, and the scanning rate was set to 0.5 Hz in order to diminish the topological overlap.[27] C-AFM measurements were performed for a wide range of external biases, up to 1.0 V in contact mode with a scanning rate of 0.5 Hz.[41] PFM was conducted in a dynamic contact mode with a scanning rate of 0.5 Hz.[42] The solar spectrum at AM 1.5 was determined by using a solar simulator (Oriel Sol 3A class AAA, Newport), and the $J−V$ curves and efficiencies were measured at a 0.03 V s$^{−1}$ scan rate.

■ ASSOCIATED CONTENT

⑤ Supporting Information

Description of the material included, including the cross-sectional image of the perovskite thin film, surface potential distribution of the films, intragrains and the GBs, topography and SEM images, $J−V$ curves of the perovskite solar cells, and SEM and EDS mapping images of the perovskite thin films. The Supporting Information is available free of charge on the ACS Publications website at DOI: 10.1021/acs.jpclett.5b00967.

■ AUTHOR INFORMATION

Corresponding Author

*E-mail: wmjo@ewha.ac.kr.

Notes

The authors declare no competing financial interest.

■ ACKNOWLEDGMENTS

■ REFERENCES

(1) Park, N.-G. Perovskite Solar Cells: An Emerging Photovoltaic Technology. *Mater. Today* **2015**, *18*, 65−72.

(2) Jung, H. S.; Park, N.-G. Perovskite Solar Cells: From Materials to Devices. *Small* **2015**, *11*, 10−25.

(3) Wang, B.; Xiao, X.; Chen, T. Perovskite Photovoltaics: A High-Efficiency Newcomer to the Solar Cell Family. *Nanoscale* **2014**, *6*, 12287−12297.

(4) Stranks, S. D.; Eperon, G. E.; Grancini, G.; Menelaou, C.; Alcocer, M. J. P.; Leijtens, T.; Herz, L. M.; Petrozza, A.; Snaith, H. J. Electron−Hole Diffusion Lengths Exceeding 1 Micrometer in an Organometal Trihalide Perovskite Absorber. *Science* **2013**, *342*, 341−344.

(5) Grätzel, M. The Light and Shade of Perovskite Solar Cells. *Nat. Mater.* **2014**, *13*, 838−842.

(6) Baikie, T.; Fang, Y.; Kadro, J. M.; Schreyer, M.; Wei, F.; Mhaisalkar, S. G.; Graetzel, M.; White, T. J. Synthesis and Crystal Chemistry of the Hybrid Perovskite $(CH_3NH_3)PbI_3$ for Solid-State Sensitized Solar Cell Applications. *J. Mater. Chem. A* **2013**, *1*, 5628−5641.

(7) Ponseca, C. S.; Savenije, T. J.; Abdellah, M.; Zheng, K.; Yartsev, A.; Pascher, T. R.; Harlang, T.; Chabera, P.; Pullerits, T.; Stepanov, A.; Wolf, J.-P.; et al. Organometal Halide Perovskite Solar Cell Materials Rationalized: Ultrafast Charge Generation, High and Microsecond-Long Balanced Mobilities, and Slow Recombination. *J. Am. Chem. Soc.* **2014**, *136*, 5189−5192.

(8) Snaith, H. J. Perovskites: The Emergence of a New Era for Low-Cost, High-Efficiency Solar Cells. *J. Phys. Chem. Lett.* **2013**, *4*, 3623−3630.

(9) Zhou, H.; Chen, Q.; Li, G.; Luo, S.; Song, T. −b.; Duan, H.-S.; Hong, Z.; You, J.; Liu, Y.; Yang, Y. Interface Engineering of Highly Efficient Perovskite Solar Cells. *Science* **2014**, *345*, 542−546.

(10) Kojima, A.; Teshima, K.; Shirai, Y.; Miyasaka, T. Organometal Halide Perovskites as Visible-Light Sensitizers for Photovoltaic Cells. *J. Am. Chem. Soc.* **2009**, *131*, 6050−6051.

(11) Green, M. A.; Ho-Baille, A.; Snaith, H. J. The Emergence of Perovskite Solar Cells. *Nat. Photonics* **2014**, *8*, 506−514.

(12) Eperon, G. E.; Stranks, S. D.; Menelaou, C.; Johnston, M. B.; Herz, L. M.; Snaith, H. J. Formamidinium Lead Trihalide: A Broadly Tunable Perovskite for Efficient Planar Heterojunction Solar Cells. *Energy Environ. Sci.* **2014**, *7*, 982−988.

(13) Tanaka, K.; Takahashi, T.; Ban, T.; Kondo, T.; Uchida, K.; Miura, N. Comparative Study on the Excitons in Lead-Halide-Based Perovskite-Type Crystals $CH_3NH_3PbBr_3$ $CH_3NH_3PbI_3$. *Solid State Commun.* **2003**, *127*, 619−623.

(14) Noh, J. H.; Im, S. H.; Heo, J. H.; Mandal, T. N.; Seok, S. I. Chemical Management for Colorful, Efficient, and Stable Inorganic−Organic Hybrid Nanostructured Solar Cells. *Nano Lett.* **2013**, *13*, 1764−1769.

(15) Chen, Q.; Zhou, H.; Song, T.-B.; Luo, S.; Hong, Z.; Duan, H.-S.; Dou, L.; Liu, Y.; Yang, Y. Controllable Self-Induced Passivation of Hybrid Lead Iodide Perovskites toward High Performance Solar Cells. *Nano Lett.* **2014**, *14*, 4158−4163.

(16) Yun, J. S.; Ho-Baillie, A.; Huang, S.; Woo, S. H.; Heo, Y.; Seidel, J.; Huang, F.; Cheng, Y.-B.; Green, M. A. Benefit of Grain Boundaries in Organic−Inorganic Halide Planar Perovskite Solar Cells. *J. Phys. Chem. Lett.* **2015**, *6*, 875−880.

(17) Yin, W.-J.; Shi, T.; Yan, Y. Unique Properties of Halide Perovskites as Possible Origins of the Superior Solar Cell Performance. *Adv. Mater.* **2014**, *26*, 4653−4658.

(18) deQuilettes, D. W.; Vorpahl, S. M.; Stranks, S. D.; Nagaoka, H.; Eperon, G. E.; Ziffer, M. E.; Snaith, H. J.; Ginger, D. S. Impact of Microstructure on Local Carrier Lifetime in Perovskite Solar Cells. *Science* **2015**, *348*, 683−686.

(19) Jeong, A. R.; Jo, W.; Jung, S.; Gwak, J.; Yun, J. H. Enhanced Exciton Separation through Negative Energy Band Bending at Grain Boundaries of $Cu_2ZnSnSe_4$ Thin-Films. *Appl. Phys. Lett.* **2011**, *99*, 082103.

(20) Kim, G. Y.; Jeong, A. R.; Kim, J. R.; Jo, W.; Son, D.-H.; Kim, D.-H.; Kang, J.-K. Surface Potential on Grain Boundaries and Intragrains of Highly Efficient $Cu_2ZnSn(S,Se)_4$ Thin-Films Grown by Two-Step Sputtering Process. *Sol. Engery Mater. Solar Cells* **2014**, *127*, 129−135.

(21) Persson, C.; Zunger, A. Anomalous Grain Boundary Physics in Polycrystalline $CuInSe_2$: The Existence of a Hole Barrier. *Phys. Rev. Lett.* **2013**, *91*, 266401/1−266401/4.

(22) Dymshits, A.; Henning, A.; Segev, G.; Rosenwaks, Y.; Etgar, L. The Electronic Structure of Metal Oxide/Organo Metal Halide Perovskite Junctions in Perovskite Based Solar Cells. *Sci. Rep.* **2015**, *5*, 8704.

(23) Jiang, C.-S.; Noufi, R.; Ramanathan, K.; AbuShama, J. A.; Moutinho, H. R.; Al-Jassim, M. M. Does the Local Built-in Potential on Grain Boundaries of $Cu(In,Ga)Se_2$ Thin Films Benefit Photovoltaic Performance of the Device? *Appl. Phys. Lett.* **2004**, *85*, 2625−2627.

(24) Jiang, C.-S.; Noufi, R.; AbuShama, J. A.; Ramanathan, K.; Moutinho, H. R.; Pankow, J.; Al-Jassim, M. Local Built-in Potential on Grain Boundaries of $Cu(In,Ga)Se_2$ Thin Films. *Appl. Phys. Lett.* **2004**, *84*, 3477−3479.

(25) Visoly-Fisher, I.; Cohen, S. R.; Gartsman, K.; Ruzin, A.; Cahen, D. Understanding the Beneficial Role of Grain Boundaries in Polycrystalline Solar Cells from Single-Grain-Boundary Scanning Probe Microscopy. *Adv. Funct. Mater.* **2006**, *16*, 649−660.

(26) Shin, R. H.; Jo, W.; Kim, D.-W.; Yun, J. H.; Ahn, S. Local Current−Voltage Behaviors of Preferentially and Randomly Textured $Cu(In,Ga)Se_2$ Thin Films Investigated by Conductive Atomic Force Microscopy. *Appl. Phys. A: Mater. Sci. Process.* **2011**, *104*, 1189−1194.

(27) Kim, G. Y.; Kim, J. R.; Jo, W.; Son, D.-H.; Kim, D.-H.; Kang, J.-K. Nanoscale Observation of Surface Potential and Carrier Transport in $Cu_2ZnSn(S,Se)_4$ Thin Films Grown by Sputtering-Based Two-Step Process. *Nanoscale Res. Lett.* **2014**, *9*, 1−5.

(28) Suarez, B.; Gonzalez-Pedro, V.; Ripolles, T. S.; Sanchez, R. S.; Otero, L.; Mora-Sero, I. Recombination Study of Combined Halides (Cl, Br, I) Perovskite Solar Cells. *J. Phys. Chem. Lett.* **2014**, *5*, 1628−1635.

(29) Wei, J.; Zhao, Y.; Li, H.; Li, G.; Pan, J.; Xu, D.; Zhao, Q.; Yu, D. Hysteresis Analysis Based on the Ferroelectric Effect in Hybrid Perovskite Solar Cells. *J. Phys. Chem. Lett.* **2014**, *5*, 3937−3945.

(30) Fan, Z.; Xiao, J.; Sun, K.; Chen, L.; Hu, Y.; Ouyang, J.; Ong, K. P.; Zeng, K.; Wang, J. Ferroelectricity of $CH_3NH_3PbI_3$ Perovskite. *J. Phys. Chem. Lett.* **2015**, *6*, 1155−1161.

(31) Kutes, Y.; Ye, L.; Zhou, Y.; Pang, S.; Huey, B. D.; Padture, N. P. Direct Observation of Ferroelectric Domains in Solution-Processed $CH_3NH_3PbI_3$ Perovskite Thin Films. *J. Phys. Chem. Lett.* **2014**, *5*, 3335−3339.

(32) Lee, J. H.; Choi, M. R.; Oh, Y. J.; Jo, W. Local Retention Behaviors of Epitaxial and Polycrystalline $PbMg_{1/3}Nb_{2/3}O_3$−$PbTiO_3$ Thin Films by Scanning Force Microscopy. *Appl. Phys. Lett.* **2007**, *91*, 072906.

(33) Kim, T. Y.; Lee, J. H.; Oh, Y. J.; Choi, M. R.; Jo, W. Charge Retention Behaviors of Preferentially Oriented and Textured $Bi_{3.25}La_{0.75}Ti_3O_{12}$ Thin Films by Electrostatic Force Microscopy. *Appl. Phys. Lett.* **2007**, *90*, 082901.

(34) Stoumpos, C. C.; Malliakas, C. D.; Kanatzidis, G. Semiconducting Tin and Lead Iodide Perovskites with Organic Cations: Phase Transitions, High Mobilities, and Near-Infrared Photoluminescent Properties. *Inorg. Chem.* **2013**, *52*, 9019−9038.

(35) Frost, J. M.; Butler, K. T.; Brivio, F.; Hendon, C. H.; van Schilfgaarde, M.; Walsh, A. Atomistic Origins of High-Performance in Hybrid Halide Perovskite Solar Cells. *Nano Lett.* **2014**, *14*, 2584−2590.

(36) Beilsten-Edmands, J.; Eperon, G. E.; Johnson, R. D.; Snaith, H. J.; Radaelli, P. G. Non-ferroelectric Nature of the Conductance Hysteresis in $CH_3NH_3PbI_3$ Perovskite-Based Photovoltaic Devices. *Appl. Phys. Lett.* **2015**, *106*, 173502.

(37) Lee, M. M.; Teuscher, J.; Miyasaka, T.; Murakami, T. N.; Snaith, H. J. Efficient Hybrid Solar Cells Based on Meso-Superstructured Organometal Halide Perovskites. *Science* **2012**, *338*, 643−647.

(38) Chen, H.-W.; Sakai, N.; Ikegami, M.; Miyasaka, T. Emergence of Hysteresis and Transient Ferroelectric Response in Organo-Lead Halide Perovskite Solar Cells. *J. Phys. Chem. Lett.* **2015**, *6*, 164−169.

(39) Han, G. S.; Chung, H. S.; Kim, B. J.; Kim, D. H.; Lee, J. W.; Swain, B. S.; Mahmood, K.; Yoo, J. S.; Park, N.-G.; Lee, J. H.; et al. Retarding Charge Recombination in Perovskite Solar Cells using Ultrathin MgO-Coated TiO_2 Nanoparticulate Films. *J. Mater. Chem. A* **2015**, *3*, 9160−9164.

(40) Kim, B. J.; Kim, D. H.; Lee, Y.-Y.; Shin, H.-W.; Han, G. S.; Hong, J. S.; Mahmood, K.; Ahn, T. K.; Joo, Y.-C.; Hong, K. S.; et al. Highly Efficient and Bending Durable Perovskite Solar Cells: Toward a Wearable Power Source. *Energy Environ. Sci.* **2015**, *8*, 916−921.

(41) Shin, R. H.; Jeong, A. R.; Jo, W. Investigation of Local Electronic Transport and Surface Potential Distribution of $Cu(In,Ga)Se_2$. *Curr. Appl. Phys.* **2012**, *12*, 1313−1318.

(42) Lee, J. H.; Shin, R. H; Jo, W. Polarization Switching and Relaxation Dynamics of Bismuth Layered Ferroelectric Thin Films: Role of Oxygen Defect Sites and Crystallinity. *Phys. Rev. B* **2011**, *84*, 094112.